EasyChair Preprint

№ XXX

DEM ANALYSIS OF CONTACT FORCES AND TRACTIVE PERFORMANCE OF RIGID WHEEL IN GRANULAR MEDIA

Bohumir Jelinek, George Mason, John Peters, Farshid Vahedifard and Jody Priddy

August 24, 2022

DEM ANALYSIS OF CONTACT FORCES AND TRACTIVE PERFORMANCE OF RIGID WHEEL IN GRANULAR MEDIA

Bohumir Jelinek[a], George L. Mason[a], John F. Peters[a], Farshid Vahedifard[b], Jody D. Priddy[c]

[a] *Center for Advanced Vehicular Systems (CAVS), Mississippi State University, Mississippi State, MS 39762*
[b] *Civil & Environmental Engineering, Mississippi State University, Mississippi State, MS 39762*
[b] *U.S. Army Engineer Research and Development Center (ERDC), Geotechnical and Structures Laboratory (GSL), Vicksburg, MS, 39180*
bj48,mason,john@cavs.msstate.edu, Jody.D.Priddy@erdc.dren.mil

Abstract
Understanding the interaction between wheel and granular media in variable loading conditions is critical for prediction of net traction of wheeled and tracked vehicles in off-road environments. A discrete element method (DEM) is used to predict net and gross traction of a rigid wheel operating in granular subgrade over a broad range of slip conditions, represented by towed, powered, and braked modes. The DEM is routinely used for modeling vehicle performance, but although simulations appear to be realistic, the accuracy of the method is often not fully established. The modeling accuracy, in this study, is assessed by comparison to physical experiments performed over a wide range of slip. The cone index, as a measure of soil strength, is simulated to allow comparison to laboratory test data. Profiles of normal and shear stresses along the contact patch are calculated and correlated with published experimental results. The location of the transition point, at which shear stress transitions from positive to negative values, is determined. In an effort to establish the boundary conditions of the DEM, average displacements, instantaneous velocities of particles, average stress and void ratio in the subgrade are presented demonstrating the greater data resolution provided by the DEM versus physical experiments. Integration of DEM and physical experiments for comprehensive models of vehicle-terrain interaction is discussed.

Keywords: Off-Road Mobility, Tractive Performance, Discrete Element Method, Rigid Wheel

1. Introduction

Use of wheels for transportation, with first wheeled wagons traced to approximately 3500 B.C. (Bakker et al. 1999), profoundly affects the life of human beings. Wheeled vehicles operate on paved roads or in more challenging off-road environments. In off-road environments, wheels commonly operate on a variety of subgrade materials, including rock, gravel, sand, silt, clay soil, or their mixtures. Characterizations of mobility in off-road environment supports advancements in agriculture, military, and space exploration.

Vehicle modeling has reached a high level of sophistication including accurate simulation of complex powertrain and suspension systems. This sophistication in not yet matched by the ability to model the interaction between the vehicle and subgrade. Wheel-soil interaction generally involves large deformation, material non-linearity, and contact mechanics that lie at the edge of both numerical modeling capabilities and the capabilities of high performance parallel computing. The discrete element method (DEM), which obviates many difficulties modeling granular subgrade media, has been used to achieve realistically looking simulations. Detailed comparisons between simulation and physical experiments are limited. Interaction between subgrade and the wheel is traditionally characterized by profiles of shear and normal stresses along the wheel surface. Knowing these stresses as a function of wheel velocity with respect to the soil (the slip) is sufficient to determine the net traction or drawbar pull, gross traction, sinkage, and slip. Normal pressure distributions under rigid wheels and slip versus sinkage relationship were experimentally studied by Hegedus (1965). Radial and shear stress distributions under rigid wheels in granular soil for varying loads and slip conditions were measured by Krick (1969). Semi-empirical models of wheel performance were then developed and compared with laboratory tests (Wong, 1967; Wong and Reece, 1967a, 1967b). Tractive performance of the pneumatic wheels in coarse and fine-grained soils was extensively measured in 1960–70's at the U.S. Army Corps Engineer Waterways Experiment Station in Vicksburg, MS (Turnage, 1972; Melzer, 1976). Data from these experiments were digitized into Database Record for Off-road Vehicle

Environments (DROVE) database (Mason et al., 2016, 2018; Vahedifard et al., 2016, 2017). Selected results will be used in this paper to assess the potential of the DEM for tire-soil interaction analysis.

Several studies used DEM to characterize the interaction of granular subgrades with rigid wheels. A two-dimensional DEM model applying non-spherical subgrade particles approximated by two-sphere clumps was used by Asaf et al. (2006) to characterize tractive performance of a rigid DEM wheel with straight bar lugs. A study by Khot et al. (2007) experimentally validated DEM model for two soil types and compared with laboratory results. Two-dimensional coupled Finite Element–DEM analysis of a wheel with solid rim and elastic surface layer in towed and powered conditions was performed by Nishiyama et al. (2016, 2018). The 2D approximation avoided large computational cost of the full 3D model at the cost of not capturing lateral variations.

In three-dimensions, the bulk of DEM work focused on predicting the mobility of rovers on Earth, the Moon, and Mars in regolith sediments (Nakashima et al. 2010; Knuth et al. 2012; Nakashima and Kobayashi 2014; Johnson et al. 2015, 2017), exploring the effects of gravity on sinkage and motion resistance of a rigid rover wheel. Zhang et al., 2015 proposed and evaluated bionic design of tread inspired by the ostrich foot that led to a 5.2 percent increase in drawbar pull performance. Tractive performance of off-road wheel on dry sand, including steering, was analyzed by Du et al. (2017a, 2017b, 2018). These studies examined the effects of lug type, intersection of lug bars, and central angle, with the objective to improve performance prediction for straight and steered performance. The scope of off-road mobility modeling was extended beyond rigid wheels by introducing finite element pneumatic tire model Recuero et al. (2017). Vertical stress under the wheels of agricultural machinery obtained from DEM using Yade (Šmilauer et al. 2015) was compared with pseudo-analytical continuum model and field measurements (De Pue et al., 2019; De Pue and Cornelis, 2019; De Pue et al., 2020).

In this work, a DEM model of a rigid wheel using spherical DEM particles with parameters from Peters et al. (2019) is evaluated. The principal goal of the research is to establish the quantitative accuracy of the tractive performance using the DEM. The secondary objective is to establish the bounding conditions for the coupled Finite Element–DEM models as examined by Nishiyama et al. (2016, 2018) and Liu et al. (2020). In particular, the research identifies when the simulation transitions from large initial transient movement to dynamic steady state and evaluates kinematics of this dynamic steady state. The contact force profile is examined in braked, towed, and powered operation. The stress profile along the contact patch is compared with experimental measurements. Average velocity of simulated particles and stress under the wheel are obtained. Relative velocity of simulated particles with respect to the wheel surface is related to the location of the shear stress transition point at which shear stress transitions from positive to negative values. The shear stress transition point separates two regions under the wheel-soil contact patch: a front region exerting torque acting to decrease the wheel rotation and a rear region acting to increase the wheel rotation. The two regions are observed in towed condition at near-zero slips. For large positive slips, the whole contact surface will act to decrease wheel rotation, while for large negative slips, the whole contact surface will act to increase wheel rotation. The areas around the tire where large discontinuous deformations occur with respect to differing wheel slip conditions is defined.

2. DEM methodology

DEM modeling technique and parameters used in this study can be found in Peters et al. (2019). DEM models the interactions among soil particles and the interactions of soil particles with rigid objects. Motions of individual particles and rigid objects are tracked, and the aggregate particle motion allows to capture large discontinuous deformations. The rigid objects in the present model, a wheel and rectangular sample container, are shown in Fig. 1. Dimensions of the container box and wheel are given in Table 1. The laboratory tests were conducted in a container 162 cm wide and 91 cm deep, but was designed for larger 152 cm diameter tires carrying 4,500 kilograms. Particles are represented by spheres. Size of particles and the wheel are shown in Table 1. Both rigid objects are represented by triangular facets which interact with the particles through contact laws similar to particle-to-particle contacts.

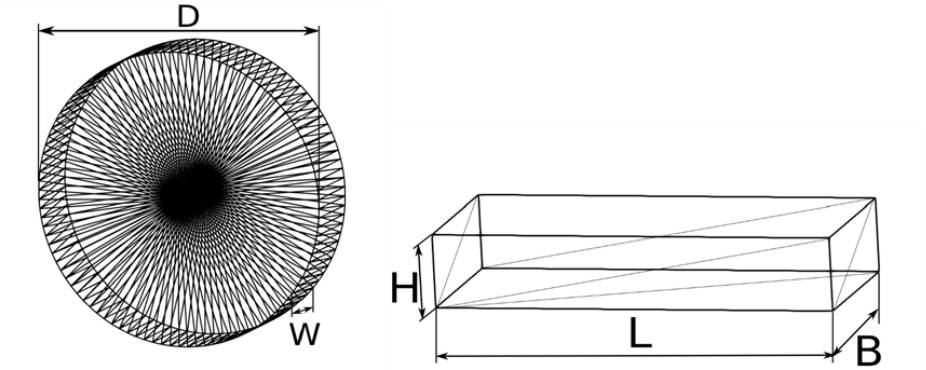

Fig. 1. Triangular facet representation of the wheel and enclosing box.

Table 1. Dimensions of the wheel, box, and particle sizes.

Property	Symbol	Units	Value
Wheel diameter	D	cm	71.27
Wheel width	W	cm	17.78
Wheel weight	F_G	N	1922
Box length	L	cm	121.92
Box width	B	cm	53.34
Box depth	H	cm	22.23
Soil depth	h	cm	20.06
Number of particles	N	-	36,037,017
Smallest particle diameter	d_{min}	mm	0.76
Largest particle diameter	d_{max}	mm	2.29
Mean particle diameter	d_{mean}	mm	1.62

The major limitation of the DEM is the computational cost of identifying particle contacts at each time step to calculate contact forces and particle displacements. This limitation is controlled by access to high performance parallel computing (HPC) resources. The number of particles in this study was 36,037,017. Particle size distribution was similar to that of Peters et al. (2019), resulting in the same soil properties. Mean DEM particle diameter of 1.62 mm was deemed sufficiently small because it demonstrated convergence of the cone index with successive particle refinement (Peters et al. 2019). With the time step of 43 ns, it took 26 hours of wall clock time to simulate 10 ms on 10 supercomputer nodes each having two Intel Xeon E5-2680 v2 ten-core CPUs. No GPUs were used in this work, and CPU computations were processor-limited compared to what is possible with current HPC technology.

3. Soil Strength

To compare the performance of the wheel to physical experiments, we first assess the subgrade soil strength simulating the cone index profile using the procedure of Peters et al. (2019). Figure 2 compares the soil strength profiles from the physical experiments by Melzer (1971) with the simulated cone index. The laboratory cone index, given by the dashed line, indicates the strength of the simulated subgrade is close to the very dense lab sample. The simulated resistance weakens with depth, but stays within the limits of the dense and very dense lab sample. The cone index profile produced from the DEM study (Fig. 2) indicates the sand is weaker than that found by Peters et al. (2019), even though the same properties were used.

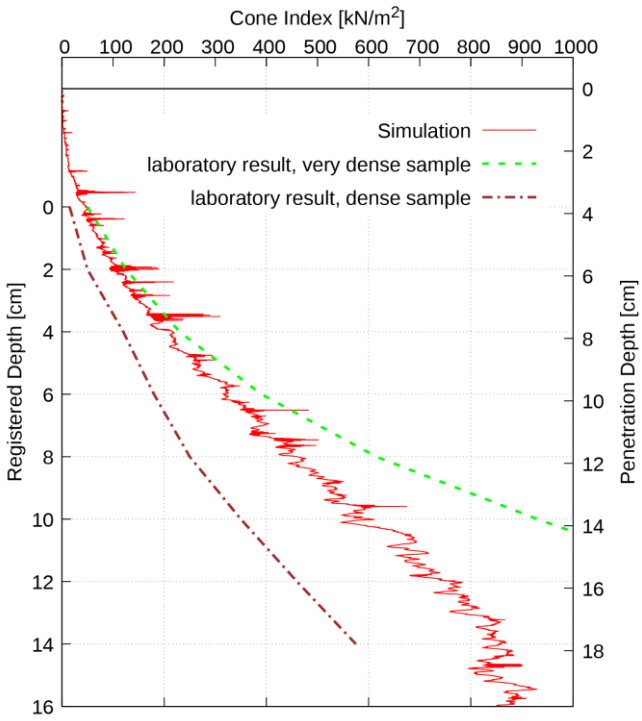

Fig. 2. Cone penetration resistance (red) compared with calibration chamber tests described in Peters et al. (2019).

4. Rolling resistance, drawbar pull, and gross tractive effort

Particles were first settled under gravity in the sample container. The wheel was then placed at a distance of 1/4 *L* and allowed to settle under gravity with the constraint that it could only move freely in the z-direction. After settling, the wheel was forced to move forward with prescribed forward velocity. The wheel was free to move vertically in response to gravity and soil reaction forces. To simulate the towed condition, the wheel was allowed to rotate freely in response to torque exerted by contact with the subgrade with no torque applied at the axle. To simulate the prescribed slip conditions (braked or powered operation), the rotational velocity of the wheel was prescribed to achieve the slip values of either -20% and 20% according to the slip definition:

$$i = 1 - \frac{v_f}{\omega r} \tag{1}$$

where i is powered slip, v_f is the forward velocity of the wheel set to 1.67 m/s (5.5 ft/s) and ω is a variable angular velocity of wheel rotation. The prescribed slip of 20 percent represents the powered mode, whereas the slip of -20 percent represents the braked mode.

The wheel-soil configuration achieved steady state after the wheel traveled for approximately 100 ms (15 cm) - when a bulldozed pile of particles reaches the final steady state shapes, as depicted in Fig. 3.

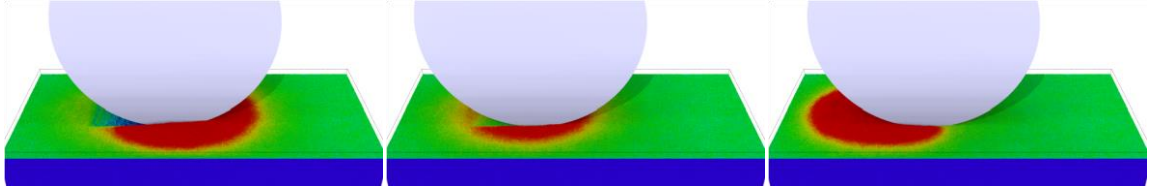

Fig. 3. Bulldozing of soil (red) by the wheel at -20%, 0%, and +20% slip. The red color corresponds to mounding particles. The wheel travels in the left-to-right direction.

After reaching the steady state, values of sinkage, pull, and gross tractive effort remain approximately constant as indicated by the time evolution shown in Fig. 4. Contact forces exerted by particles on the wheel were measured and used to calculate total pull force F_x and gross tractive effort T as a sum of contributions from particles j in contact with the wheel:

$$F^x = \sum_j F_j^x, \tag{2}$$

$$T = \frac{1}{D/2}\sum_j F_j^t d_j = \sum_j F_j^t, \tag{3}$$

where F^x is the forward component of the contact force, F^t is the wheel-surface-tangential component of the contact force, D is the wheel diameter and d_j is distance from the contact point to the wheel axis. F^t has negative/positive sign if the force acts to increase/decrease wheel rotation.

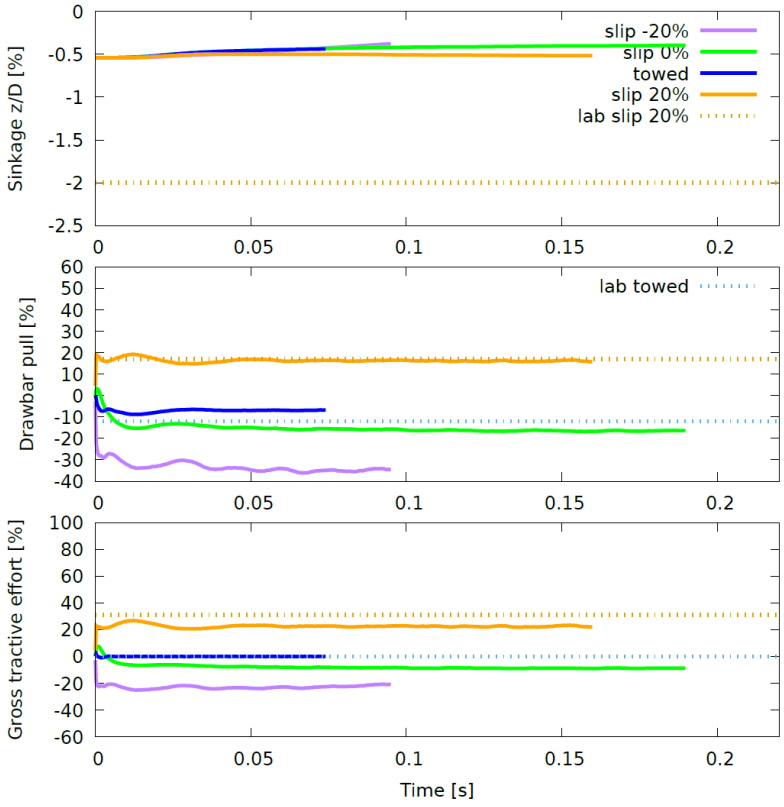

Fig. 4. Time evolution of sinkage, pull, and gross tractive effort coefficients at -20%, towed, 0%, and 20% slip conditions. Pull and tractive effort are normalized by the wheel weight F_g.

The dashed lines in Fig. 4 indicate the experimental results from lab tests on the smooth solid rubber 71.27 cm diameter tire with circular profile. Numerical results and their agreement with experiments will be discussed in the following sections.

5. Averaging

Averages were obtained from the region under the wheel width using binning in Cartesian and wheel-centered cylindrical coordinates. The bin size was 6.35 mm × 6.35 mm × 17.78 cm for Cartesian binning. Such a bin size resulted in

approximately 2000 particles per bin with the particle size range in Table 1. A single bin corresponds to a single colored square in Fig. 12. For cylindrical binning, angular interval was 2° and radial displacement of bin centers was 6.35 mm. Starting points of arrows in Fig. 5 are located in bin centers.

6. Velocities of particles

Defining areas of high and low particle velocity between the tire and soil interface is important in optimum tire design and loading. When wheel operates on a solid surface, the slip between the wheel and subgrade is limited the wheel-surface contact area. On a granular subgrade the slip between the wheel and subgrade extends into the layers of soil near the contact patch. Depth of the displaced soil depends on the soil parameters and on the wheel surface friction. Low displacement rates indicate boundaries where nearly-elastic state of soil occurs below the wheel. Figure 5 shows averaged particle velocities under the wheel. The forward velocity of the wheel at each slip is indicated by the topmost black arrow. The rim velocity is indicated by three arrows: first on the left side of the rim, second on the right slide of the rim, and the velocity of the bottom-most point of the rim is indicated by an arrow placed between the bottom-most point of the rim and the forward-velocity arrow.

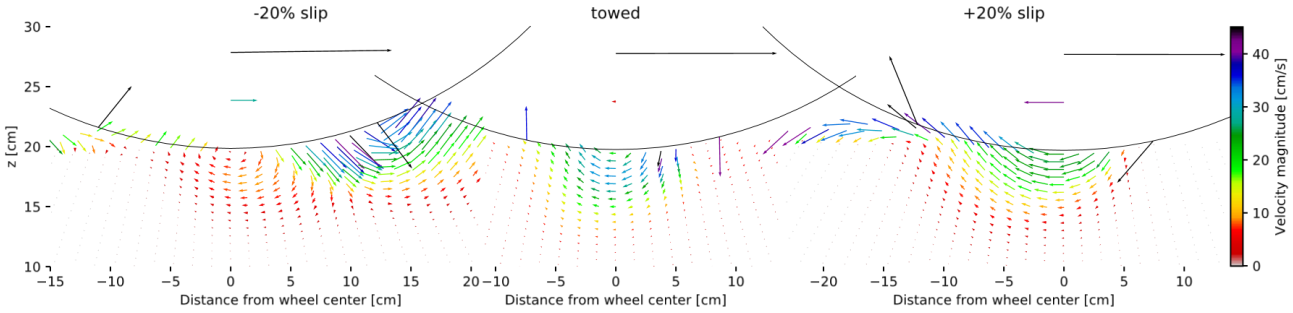

Fig. 5. Averaged particle velocities under the 0.71-meter wheel at the steady state in braked (-20% slip), towed, and powered (20% slip) conditions.

Particle displacement rate decreased significantly 5 cm below the soil/wheel contact. Displacement during negative slip or braking primarily occurred 20 cm in front of the wheel whereas during positive slip, or powered mode, high particle velocities were observed 20 cm behind the wheel. During the towed mode high particle velocities occurred primarily beneath the wheel/soil interface at a depth of 5 cm.

Overall, the particle flow pattern qualitatively agrees with experimental observations obtained at the slip of −30% and 30% by Senatore et al. (2013); Senatore and Iagnemma (2014). The present DEM model produced smaller region of forward flow than experimentally observed by Skonieczny et al. (2014) and Inotsume et al. (2019), likely due to higher sinkage in their experiments.

Figure 6 shows particle velocity between the contact patch of the wheel and the soil. The flow lines agree with directions of shear stress at 40% slip as presented by Higa et al. (2015b). High particle velocities are observed across the entire contact area of the wheel in the powered mode. The region of particle movement is limited in the towed mode and during the braked mode, the high particle velocities are observed on the leading edge of the wheel. Using these observed particle velocity patterns, tread orientation could be set perpendicular to the velocities to limit slip at the tire-wheel interface, and thus to optimize net traction. Due to the rectangular profile of the wheel, the flow is mostly observed in forward and backward directions. For a circular tire profile, more intense flow towards the sides of wheel would be observed.

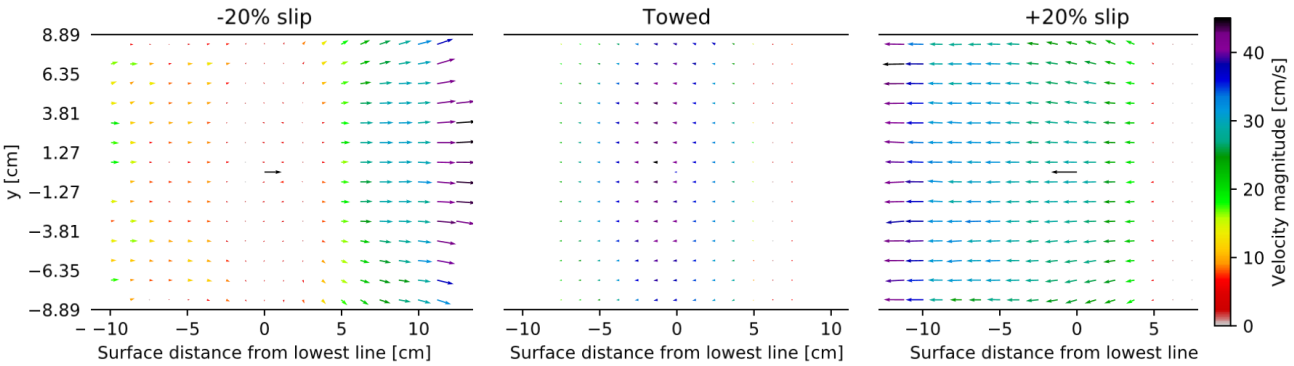

Fig. 6. Averaged tangential velocities of particles near the wheel surface in braked (-20% slip), towed, and powered (20% slip) conditions.

7. Stress under the wheel

The soil stress is an important engineering quantity difficult to measure in physical experiments but obtainable at high resolution in numerical analyses. The stress is obtained from the DEM by first computing the so called particle stress for each particle, which can then be averaged over a finite sampling volume. The particle stress is computed for each particle (particle p) based on the N_c forces made with contacting particles (particles q), as given by

$$\sigma_{ij}^{p} = \frac{1}{V_P} \sum_{q=1}^{N_c} r_i^{pq} f_j^{pq}, \tag{4}$$

where V_p is the volume of the particle p, r_i^{pq} is the i-th component of the vector $\boldsymbol{r}^{pq}$ that connects the particle center to the contact, f_j^{pq} is the j-th component of a contact force between the two particles, and the sum is performed over the number of contacts N_c of the particle p. For spherical particles, r^{qp} lies in the direction of the vector connecting centers of particles p and q. The particle stress is then averaged over Cartesian bins

$$\sigma_{ij}^{b} = \frac{1}{V_b} \sum_{q=1}^{N_b} V_p \sigma_{ij}^{p}, \tag{5}$$

where V_b is the volume of the bin, and the sum is performed over the N_b of particles within the bin b. Bin shapes and sizes are specified in Section 5. The depth of each bin is equal to the wheel width W.
Vertical and shear stress components are shown in Fig. 7, illustrating a side view of the wheel.

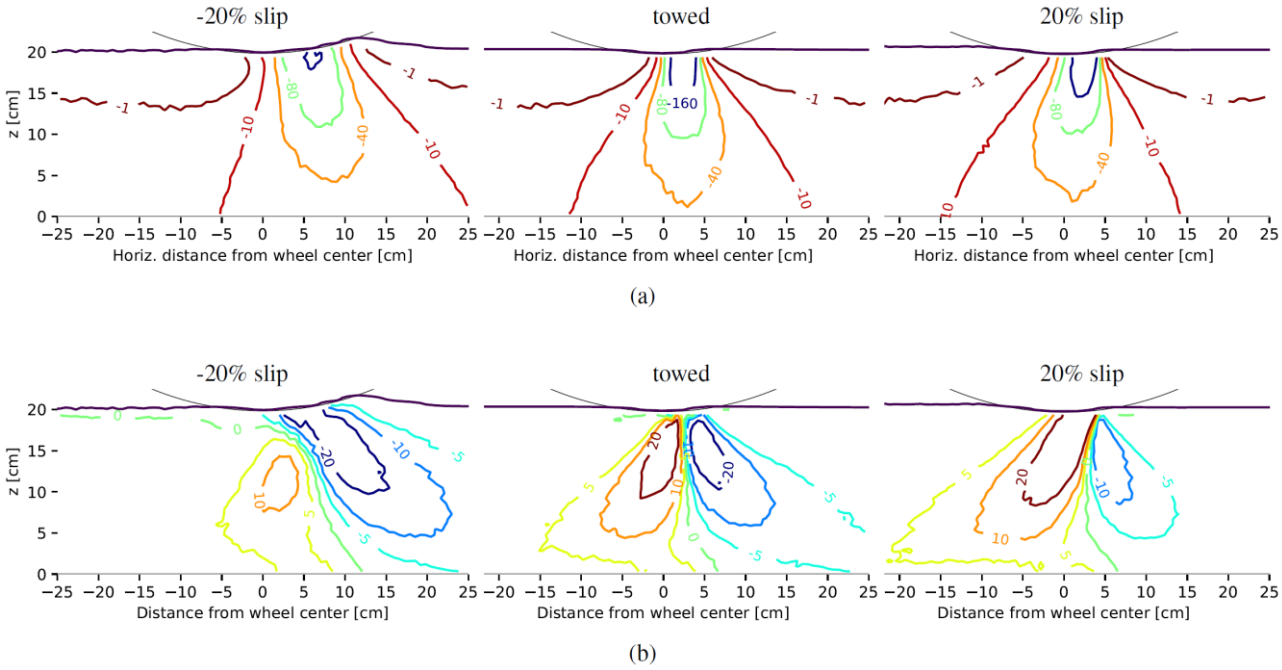

Fig. 7. Longitudinal variation of (a) vertical and (b) shear stress under the wheel in braked (-20% slip), towed, and powered (20% slip) conditions in kPa. Side view of wheel traveling in the left-to-right direction.

The side view of the vertical stress indicates the angle of the pressure bulb depends on the wheel slip. The pressure bulb is directly underneath the wheel in the powered mode, but shifts towards the leading edge of the wheel during the braked mode. Figure 8 illustrates a forward looking view of the wheel. The front view of the wheel indicates a nearly symmetrical pressure bulb that exerts higher vertical pressures with depth as the wheel goes from braked to powered mode. Vertical pressure directly under the wheel increases due to the changing angle of the pressure bulb as seen in the side view (Fig. 7). The vertical stress is symmetric in the towed mode, with high stress concentrated in front of the wheel during braking and behind the wheel during the powered mode, once again due to the change in the orientation of the pressure bulb.

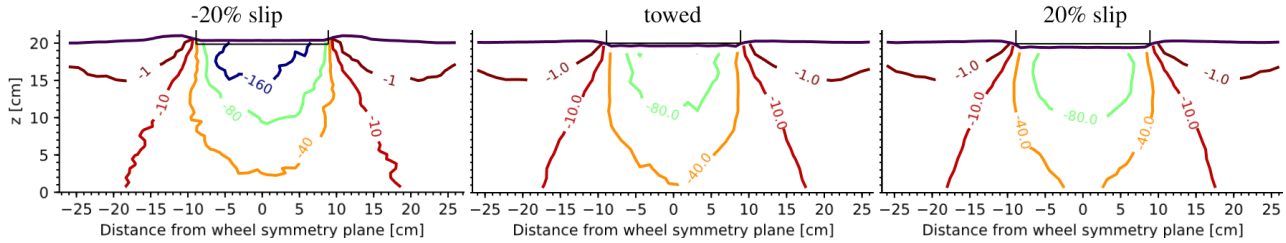

Fig. 8. Lateral variation of vertical stress under the wheel in braked (-20% slip), towed, and powered (20% slip) conditions in kPa. Front view of the wheel. Braked values are from a lateral plane passing through wheel axis of rotation inclined 10° from the downward direction.

Distribution of normal stress along the contact patch is shown in Fig. 9. Tire inflation pressure significantly affects the tractive performance of a wheel. Unlike the pneumatic tire, a rigid wheel will not adjust the shape according to the pressure from subgrade. When a pneumatic tire is driven on a firm surface, high inflation pressure will lead to decreased net traction and excessive wear in the middle of the tire profile. When driven on the granular surface, the effect of tire pressure on tractive performance is even more pronounced, and the wear is harder to predict. The present rigid wheel DEM model does not provide a good representation of the pressure distribution along the surface of a pneumatic tire unless the inflation pressure is high. However, the model shows that normal stress is largest in the middle of the rigid wheel contact surface what agrees with experimental observation by Hegedus (1965).

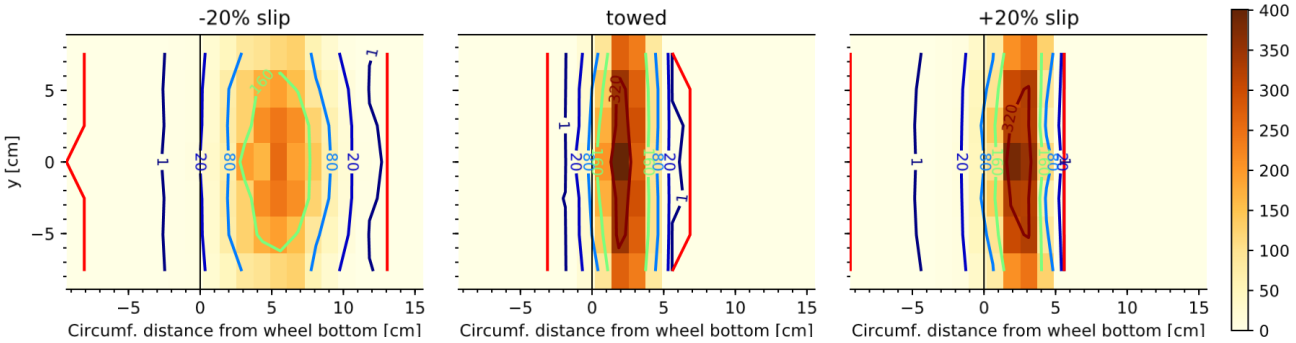

Fig. 9. Variation of normal stress along the contact patch in braked (-20% slip), towed, and powered (20% slip) conditions. The wheel travels to the right.

8. Normal and shear forces and stress profile on the wheel surface

Motion of a single driven wheel is initiated by a torque originating from the wheel propelling mechanism. Torque, however, only results in the wheel rotation. For the wheel to accelerate forward, the net force acting on the wheel must point forward. The forward force on the driven wheel is a result of frictional reaction of the subgrade to the wheel rotation. Without subgrade friction, the wheel would spin without forward motion. Horizontal component of the subgrade reaction causes forward acceleration of the wheel, whereas the vertical component of the subgrade reaction balances the gravitational force.

Figure 10 shows normal and shear stress profiles and soil reaction forces along the wheel-soil interface. Normal and shear stress distributions are similar to those experimentally measured on the surface of rigid wheels Krick (1969). Peak of the normal stress is in the leading region of the contact area in agreement with experimental measurements by Higa et al. (2015a). At the steady state, the vertical component of the soil reaction force is balanced by gravity, whereas the horizontal component is balanced by the towed load. Similarly, the tangential components of the soil reaction forces are compensated by applied torque. Smaller black arrows represent total forces acting on angular sections of the contact patch, whereas the largest black arrow is a total force exerted by particles on the wheel. The large green arrow is a sum of normal forces, the red arrow is a sum of shear forces.

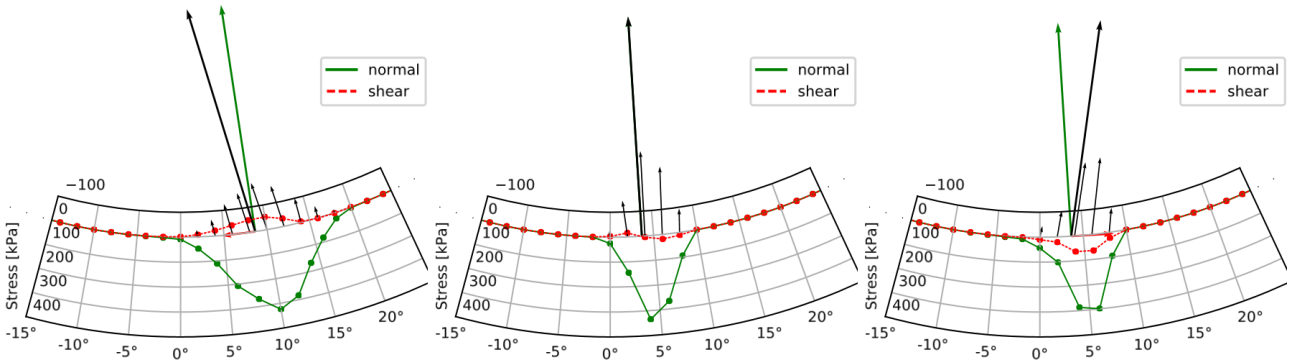

Fig. 10. Simulated radial and shear stress profile at the steady state in braked (-20% slip), towed, and powered (20% slip) conditions. Vertical component of the largest black arrow corresponds to wheel weight, which is 1992 N.

8.1 Slip at wheel-soil interface

Gross traction, representing torque input required to power or break the wheel, is proportional to a sum of shear forces acting on the outer surface of the wheel. The shear forces on the wheel surface include static and dynamic friction. Friction depends on the magnitude of normal force and on the direction of the velocity of particles relative to wheel surface. Figure 11 shows shear stress profile and velocities of particles relative to the wheel surface. Two velocity curves correspond to the relative velocity at particle centers and at the particles-wheel contact points. The shear stress on the

wheel surface is positive when a particle acts to decelerate the wheel rotation, or negative when the particle acts to accelerate the wheel rotation. It can be seen that the shear stress is positive when the relative velocity is positive (20 percent slip) and it is negative when the relative velocity is negative (-20 percent slip). In towed conditions, the transition point (sign change) of the shear stress coincides with the sign change of the relative velocity at contact points.

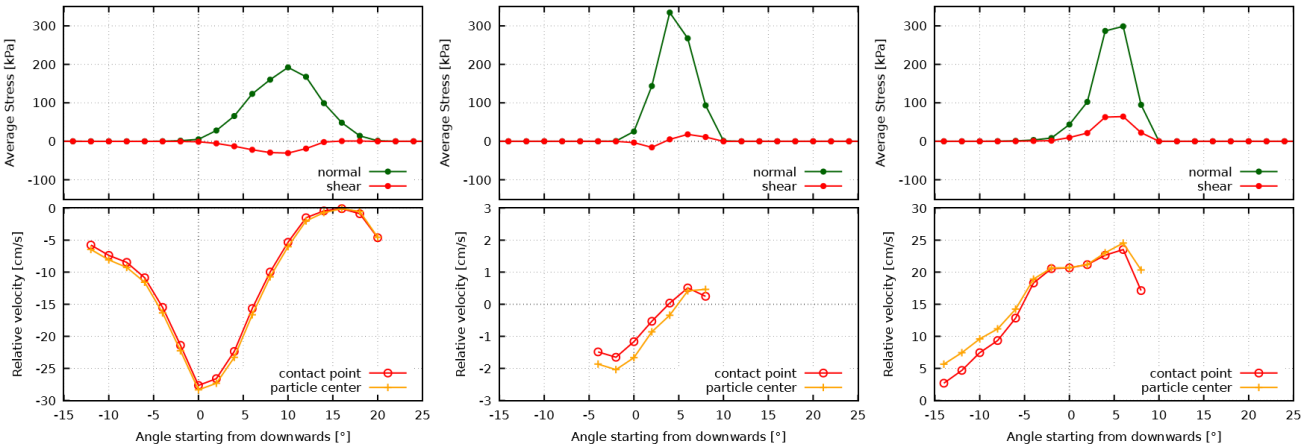

Fig. 11. Relationship of tangential velocity of particles with respect to wheel surface and shear stress for -20% slip, towed, and 20% slip wheel.

9. Void ratio

The void ratio before and after traffic is an indication of where changes in the soil properties occur that could become locations of subgrade degradation. Porosity in the subgrade was evaluated as

$$\phi_b = 1 - \frac{\sum_{\mathbf{r}_p \in V_b} V_p}{V_b}. \tag{6}$$

where the V_b is the volume of the bin, as in Eq. 5, V_p is the volume of the particle p, and the sum is performed over the particles with center within the bin, $\mathbf{r}_p \in V_b$. Void ratio was then evaluated as $e_b = \phi_b/(1 - \phi_b)$. Figure 12 shows void ratio under the wheel, with the wheel traveling from left to right. The initial void ratio distribution is similar to that to the right of the wheel, which is yet to be disturbed. The majority of porosity changes occur between the wheel and soil interface during braked and powered conditions. The void ratio appears unchanged at a depth of 10 cm below the wheel surface or 14 percent of the wheel diameter. This disturbance depth, however, is specific for the slip up to 20 percent, the wheel diameter 70 cm, and the wheel load of 1922 N.

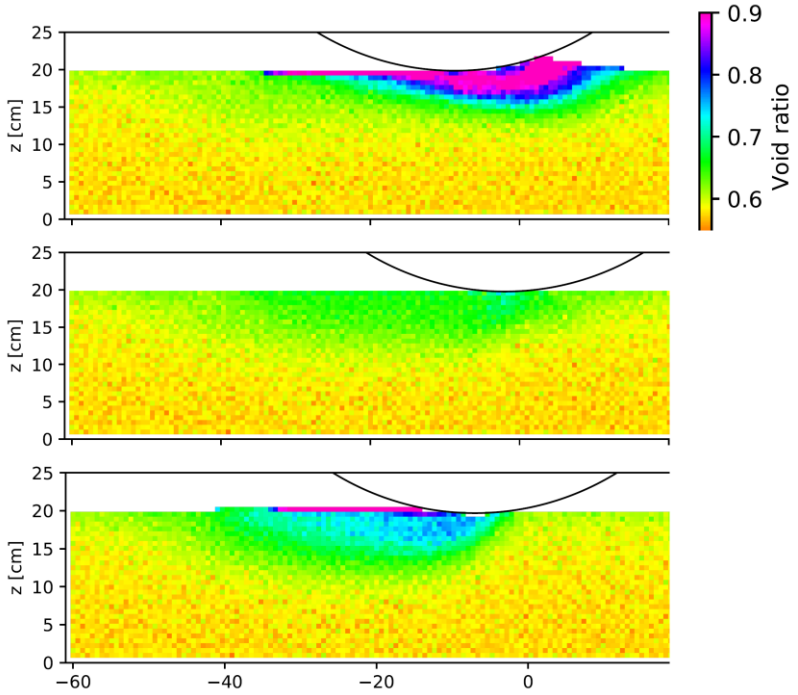

Fig. 12. Void ratio under the wheel in braked (-20% slip), towed, and powered (20% slip) conditions.

10. Tractive performance

Comparison between DEM simulation results and laboratory experiment of drawbar pull (net traction) and gross traction for 71.12 cm diameter smooth solid rubber tire in sand are given in Table 2. These results are obtained for an experimental 0-15 cm average cone index CI= 400 kPa using the procedure described in McRae et al. (1965).

Table 2. Laboratory test results for solid rubber tire with diameter 71.27 cm and 17.78 cm width vs. rigid DEM wheel.

Conditions			20% slip		Towed	
	Pull [%]		Gross tractive effort [%]		Pull [%]	
	Lab.	DEM	Lab.	DEM	Lab.	DEM
Results	17	15	31	20	-12	-8

The simulated drawbar pull at 20 percent slip was 2 percent lower than the experiment whereas the simulated gross traction was 11 percent lower than the experiment. The simulated value for pull in towed mode was 6 percent lower than the experiment. The laboratory drawbar pull and gross traction was measured higher than the respective DEM results. Tractive performance obtained using DEM compared well with the laboratory test for a wheel with the rolling radius of 41.3 cm and 8230 N load as shown in Fig. 13. The gross traction measured in the laboratory is depicted by the blue line in Fig. 13 along with the net traction illustrated by the red line. The difference in the gross and net traction is the motion resistance and it partly depends on the sinkage. The DEM results are depicted by the markers in Fig. 13 with the circles as gross traction and the plus as net traction. The motion resistance or difference in net and gross traction is significantly less for the DEM results. The poor estimate of motion resistance is likely the result of significant under prediction of sinkage considering that the sinkage is the principal source of resistance in this experimental set up. The sinkage of the tire (Fig. 4) did not match the laboratory results. The poor sinkage estimate is possibly the result of the simulated wheel having rectangular profile whereas the experimental tire had circular profile. Moreover, the simulated sample box is relatively shallow compared to physical experiments for which the sample box depth was 91 cm (Section 2). The depth of soil was shallow with respect to the wheel diameter and weight. The number of particles and therefore soil volume was

limited so that the simulation can finish within reasonable time. The dimensions of the simulated box were constrained by available HPC resources.

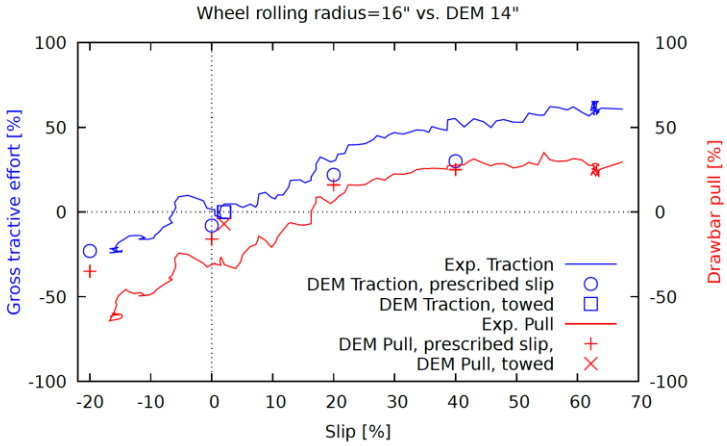

Fig. 13. Pull and gross tractive effort coefficient versus slip.

11. Conclusions

A solid rubber tire was modeled with a high resolution DEM over a coarse grain media and compared to laboratory tests. The study was conducted to evaluate pressure distributions, change in soil state under and around the tire, and compare gross tractive force/slip for one soil strength. The data suggests that beyond 14 percent of the tire diameter, significant changes in the consolidation state of the soil do not occur. The change in particle velocity was observed at a depth of no more than 7 percent below the tire/soil interface. Significant particle velocities were observed in front and behind the tire no farther than 28 percent of the tire diameter, as measured from the center of the tire for braked and powered scenarios respectively. These data suggest the regions where the computationally intensive DEM model will benefit the analysis. The tractive force/slip curves suggest that sinkage and therefore motion resistance is not represented through the DEM model. We believe that boundary conditions on the side and bottom of the box may influence the displacement.

Nomenclature

B	Box width	[m]
D	Wheel diameter	[m]
H	Box depth	[m]
F^x	Forward component of force on wheel	[N]
F_G	Wheel weight	[N]
F_j^t	Wheel-surface-tangential component of the wheel contact force with particle j	[N]
F_j^x	Forward component of force on particle j	[N]
L	Box length	[m]
N	Number of particles	[]
N_b	Number of particles within the bin b	[]
T	Gross tractive effort	[Nm]
V_p	Volume of the particle p	[m^3]
V_b	Volume of the bin b	[m^3]
W	Wheel width	[m]
d_j	distance from the j-th particle wheel contact point to the wheel axis	[m]
d_{min}	Smallest particle diameter	[m]
d_{max}	Largest particle diameter	[m]

d_{mean}	Mean particle diameter	[m]
H	Soil depth	[m]
I	Wheel slip	[]
R	Wheel radius	[m]
r_i^{pq}	i-th component of the vector $\boldsymbol{r}^{pq}$ that connects the particle center to the contact	[m]
$\boldsymbol{r}_p$	Position vector of particle p	[m, m, m]
v_f	Forward component of wheel velocity	[m/s]
ϕ_b	Porosity in the subgrade within the bin b	[]
ω	Angular velocity of wheel rotation	[rad/s]
σ_{ij}^p	i, j component of particle stress	[N/m^2]
σ_{ij}^b	Volume-averaged stress	[N/m^2]

Acknowledgements

This material is based upon research conducted under contract W9I2HZ-17-C-0021 with the U.S. Army Engineer Research and Development Center (ERDC). The views and conclusions contained herein are those of the authors and should not be interpreted as necessarily representing the official policies or endorsements, either expressed or implied, of ERDC or the U.S. Government. Distribution Statement A; Approved for public release: distribution unlimited.

References

Asaf, Z., Shmulevich, I., Rubinstein, D., 2006. Predicting soil-rigid wheel performance using distinct element methods. Transactions of the ASABE 49, 607.

Bakker, J.A., Kruk, J., Lanting, A.E., Milisauskas, S., 1999. The earliest evidence of wheeled vehicles in Europe and the Near East. Antiquity 73, 778–790.

De Pue, J., Cornelis, W.M., 2019. DEM simulation of stress transmission under agricultural traffic Part 1: Comparison with continuum model and parametric study. Soil and Tillage Research 195, 104408.

De Pue, J., Di Emidio, G., Verastegui Flores, R.D., Bezuijen, A., Cornelis, W.M., 2019. Calibration of DEM material parameters to simulate stress-strain behaviour of unsaturated soils during uniaxial compression. Soil and Tillage Research 194, 104303.

De Pue, J., Lamande, M., Schjønning, P., Cornelis, W.M., 2020. DEM simulation of stress transmission under agricultural traffic Part 3: Evaluation with field experiment. Soil and Tillage Research 200, 104606.

Du, Y., Gao, J., Jiang, L., Zhang, Y., 2017a. Numerical analysis of lug effects on tractive performance of off-road wheel by DEM. Journal of the Brazilian Society of Mechanical Sciences and Engineering 39, 1977–1987.

Du, Y., Gao, J., Jiang, L., Zhang, Y., 2017b. Numerical analysis on tractive performance of off-road wheel steering on sand using discrete element method. Journal of Terramechanics 71, 25–43.

Du, Y., Gao, J., Jiang, L., Zhang, Y., 2018. Development and numerical validation of an improved prediction model for wheel-soil interaction under multiple operating conditions. Journal of Terramechanics 79, 1–21.

Hegedus, E., 1965. Pressure distribution under rigid wheels. Transactions of the ASAE 8, 305–308.

Higa, S., Nagaoka, K., Nagatani, K., Yoshida, K., 2015a. Measurement and modeling for two-dimensional normal stress distribution of wheel on loose soil. Journal of Terramechanics 62, 63–73.

Higa, S., Sawada, K., Nagaoka, K., Nagatani, K., Yoshida, K., 2015b. Three-dimensional stress distribution on a rigid wheel surface for a lightweight vehicle, in: Proceedings of the 13th European Conference of the ISTVS, pp. 383–391.

Inotsume, H., Moreland, S., Skonieczny, K., Wettergreen, D., 2019. Parametric study and design guidelines for rigid wheels for planetary rovers. Journal of Terramechanics 85, 39–57.

Johnson, J.B., Duvoy, P.X., Kulchitsky, A.V., Creager, C., Moore, J., 2017. Analysis of Mars Exploration Rover wheel mobility processes and the limitations of classical terramechanics models using discrete element method simulations. Journal of Terramechanics 73, 61–71.

Johnson, J.B., Kulchitsky, A.V., Duvoy, P., Iagnemma, K., Senatore, C., Arvidson, R.E., Moore, J., 2015. Discrete element method simulations of Mars Exploration Rover wheel performance. Journal of Terramechanics 62, 31–40.

Khot, L.R., Salokhe, V.M., Jayasuriya, H.P.W., Nakashima, H., 2007. Experimental validation of distinct element simulation for dynamic wheel–soil interaction. Journal of Terramechanics 44, 429–437.

Knuth, M.A., Johnson, J.B., Hopkins, M.A., Sullivan, R.J., Moore, J.M., 2012. Discrete element modeling of a Mars Exploration Rover wheel in granular material. Journal of Terramechanics 49, 27–36.

Krick, G., 1969. Radial and shear stress distribution beneath rigid wheels and pneumatic tyres on yielding soils with regard to tyre deformation. Journal of Terramechanics 6, 73–98.

Liu, T., Liang, L., Zhao, Y., Cao, D., 2020. Equivalent boundary model of lunar soil drilling simulation by DEM. Journal of Terramechanics 91, 85–95.

Mason, G.L., Vahedifard, F., Robinson, J.D., Howard, I.L., McKinley, G.B., Priddy, J.D., 2016. Improved sinkage algorithms for powered and unpowered wheeled vehicles operating on sand. Journal of Terramechanics 67, 25–36.

Mason, G.L., Williams, J.M., Vahedifard, F., Priddy, J.D., 2018. A unified equation for predicting traction for wheels on sand over a range of braked, towed, and powered operations. Journal of Terramechanics 79, 33–40.

McRae, J.L., Powell, C.J., Wismer, R.D., 1965. Performance of Soils Under Tire Loads. Report 1, Test Facilities and Techniques. Technical Report 3-666. U. S. Army Engineer Waterways Experiment Station, Vicksburg, MS. Vicksburg, Miss.

Melzer, K.J., 1971. Measuring Soil Properties in Vehicle Mobility Research. Report 4. Relative Density and Cone Penetration Resistance. Technical Report 3-652. U. S. Army Engineer Waterways Experiment Station, Vicksburg, MS.

Melzer, K.J., 1976. Power requirements for wheels operating in sand. Journal of Terramechanics 13, 75–85.

Nakashima, H., Fujii, H., Oida, A., Momozu, M., Kanamori, H., Aoki, S., Yokoyama, T., Shimizu, H., Miyasaka, J., Ohdoi, K., 2010. Discrete element method analysis of single wheel performance for a small lunar rover on sloped terrain. Journal of Terramechanics 47, 307–321.

Nakashima, H., Kobayashi, T., 2014. Effects of gravity on rigid rover wheel sinkage and motion resistance assessed using two-dimensional discrete element method. Journal of Terramechanics 53, 37–45.

Nishiyama, K., Nakashima, H., Yoshida, T., Ono, T., Shimizu, H., Miyasaka, J., Ohdoi, K., 2016. 2D FE–DEM analysis of tractive performance of an elastic wheel for planetary rovers. Journal of Terramechanics 64, 23–35.

Nishiyama, K., Nakashima, H., Yoshida, T., Shimizu, H., Miyasaka, J., Ohdoi, K., 2018. FE-DEM with interchangeable modeling for off-road tire traction analysis. Journal of Terramechanics 78, 15–25.

Peters, J.F., Jelinek, B., Goodman, C., Vahedifard, F., Mason, G., 2019. Large-scale discrete-element modeling for engineering analysis: Case study for the mobility cone penetrometer. Journal of Geotechnical and Geoenvironmental Engineering 145, 04019111.

Recuero, A., Serban, R., Peterson, B., Sugiyama, H., Jayakumar, P., Negrut, D., 2017. A highfidelity approach for vehicle mobility simulation: Nonlinear finite element tires operating on granular material. Journal of Terramechanics 72, 39–54.

Senatore, C., Iagnemma, K., 2014. Analysis of stress distributions under lightweight wheeled vehicles. Journal of Terramechanics 51, 1–17.

Senatore, C., Wulfmeier, M., Vlahinic, I., Andrade, J., Iagnemma, K., 2013. Design and implementation of a particle image velocimetry method for analysis of running gear–soil interaction. Journal of Terramechanics 50, 311–326.

Skonieczny, K., Moreland, S., Asnani, V.M., Creager, C.M., Inotsume, H., Wettergreen, D., 2014. Visualizing and analyzing machine-soil interactions using computer vision. J. Field Robotics 31, 820–836.

Turnage, G.W., 1972. Performance of soils under tire loads. Report 8. Application of test results to tire selection for off road vehicles. Technical Report 3-666. U. S. Army Engineer Waterways Experiment Station, Vicksburg, MS.

Vahedifard, F., Robinson, J.D., Mason, G.L., Howard, I.L., Priddy, J.D., 2016. Mobility algorithm evaluation using a consolidated database developed for wheeled vehicles operating on dry sands. Journal of Terramechanics 63, 13–22.

Vahedifard, F., Williams, J.M., Mason, G.L., Howard, I.L., Priddy, J.D., 2017. Development of a multi-year database to assess off-road mobility algorithms in fine-grained soils. International Journal of Vehicle Performance 3, 3–18.

Šmilauer, V., et al., 2015. Yade Documentation 2nd ed. The Yade Project. http://yadedem.org/doc/.

Wong, J.Y., 1967. Behaviour of soil beneath rigid wheels. Journal of Agricultural Engineering Research 12, 257–269.

Wong, J.Y., Reece, A.R., 1967a. Prediction of rigid wheel performance based on the analysis of soil-wheel stresses part I. Performance of driven rigid wheels. Journal of Terramechanics 4, 81–98.

Wong, J.Y., Reece, A.R., 1967b. Prediction of rigid wheel performance based on the analysis of soil-wheel stresses: Part II. Performance of towed rigid wheels. Journal of Terramechanics 4, 7–25.

Zhang, R., Luo, G., Xue, S., Yang, M., Liu, F., Zhang, S., Pan, R., Li, J., 2015. Transactions of the Chinese Society of Agricultural Engineering. volume 31/3. chapter Bionic design of configuration of rigid wheel moving on sand and numerical analysis on its traction performance. pp. 122–128.